Korean J. Chem. Eng., 35(12), 2355-2364 (2018)
DOI: 10.1007/s11814-018-0171-0

pISSN: 0256-1115
eISSN: 1975-7220

Simulation analysis on the separation characteristics and motion behavior of particles in a hydrocyclone

Yanxia Xu, Bo Tang, Xingfu Song†, Ze Sun, and Jianguo Yu

National Engineering Research Center for Integrated Utilization of Salt Lake Resources,
East China University of Science and Technology, Shanghai 200237, China
(*Received 5 February 2018 • accepted 15 October 2018*)

Abstract−We evaluated the effect of particle size and associated dynamics on a hydrocyclone separation process in order to understand the movement of the particle trajectories inside the hydrocyclone via numerical analysis, with particles of acid hydrolysis residues discharged in TiO_2 production via the sulfate method as a case study. The values obtained from the numerical simulation were successfully compared with those from experimental tests in the literature, allowing a description of the dynamics of the particles, their acting forces, and their relevant properties together with separation efficiency. The results showed that particle motion is jointly controlled by the drag force, the pressure gradient force and the centrifugal force. With increasing particle size, the influence of the drag force is weakened, whereas that of the centrifugal force and pressure gradient is strengthened. Factors including particle density, slurry viscosity, and inlet slurry flow rate also contribute to a clear and useful understanding of particle motion behavior in the hydrocyclone as a method for improving the separation efficiency.

Keywords: Hydrocyclone, Separation Characteristic, Particle Motion, Computational Fluid Dynamic

INTRODUCTION

The hydrocyclone is an effective device for the separation of solid/liquid mixtures and classification of particles based on densities and sizes [1,2]. In general, the partition curve is used to characterize the separation performance, which is defined by the fraction of a specific size in the feed relative to the underflow (spigot), and the sharpness, which describes the accuracy and completeness of separation. Theoretically, the partition curve decreases monotonically with the particle size of the standard curve, whereas the desired curve represents the highest separation sharpness, meaning that all of the fine particles (smaller than the cut size) are discharged through the vortex finder, and the spigot collects the coarse particles (larger than the cut size). Nevertheless, misplaced particles in both streams result in low separation efficiency and unsatisfactory sharpness of the hydrocyclone in practical application [3,4].

The most common approach to improving the separation efficiency is to optimize the structural dimensions, including the body diameter [5], inlet shape and size [6-9], vortex finder structure and size [10,11] and the cylindrical height [12]. An alternative to estimating the performance is described by Kilavuz et al. [13], who used the Do/Du ratio governing several important parameters for hydrocyclone design and optimization. Additionally, Silva et al. [14] applied the differential evolution (DE) algorithm to obtain an optimized geometry for a filtering hydrocyclone with maximum efficiency. Later, Ghodrat et al. [15] found that a longer conical section length could lead to a decreased inlet pressure drop, cut size d_{50}, Ecart probability E_p, and increased water split. The vortex finder was designed to reduce the contrary effects of short-circuit flow [16] and multiply the possibilities and applications of hydrocyclones. Vieira et al. [17] compared the performance of conventional and filtering hydrocyclones, and found a correlation between the separation performance and the capacity together with significant enhancement by a conical filtering wall. Chu et al. [18] improved the efficiency of the hydrocyclone by extending a winged core fixed below the vortex finder to control the internal turbulence structure. In another application, Bai et al. [19] removed the catalyst particles from the oil slurry by changing the cone angle and vortex finder. In a computational fluid dynamics (CFD) study, Hwang et al. [20] showed a correlation between the separation efficiency and the enlarging section of the underflow or the respective reduction of the section for the overflow diameter. The particles were efficiently separated by 20 mm hydrocyclones adapted with a conical top-plate [21]. Zhao et al. [22] designed an inner-cone structure to supply a more stable flow field for phase separation. Fu et al. [23] and Liu et al. [24] designed a device positioned prior to the inlet that arranges the inlet position of the particles with different sizes to improve the efficiency.

However, the simple geometry and operation of the hydrocyclone obscures deep flow field knowledge of the fluid mechanism and the structural configurations, significantly affecting the separation performance. Experimental and simulation methods were used to calculate the flow patterns and particle movement inside the hydrocyclone [25,26]. With respective use of high-speed motion analysis and positron emission particle tracking, Wang et al. [27] and Chang et al. [28] found a complex flow pattern of the particles inside the hydrocyclone. In the early stage, Nageswararao [29] thought that the occurrence of the fish-hook effect in hydrocyclone classifi-

†To whom correspondence should be addressed.
E-mail: xfsong@ecust.edu.cn

ers was sporadic and random under identical conditions. Patil et al. [30], on fish-hook effect occurrence, showed that particle sizes dominated the separation performance via the feed size distribution and the solid final concentration, which were dependent on the design variables. In another study, the particle displacement in the radial direction due to the centrifugal effect determined the partial separation efficiency of coarse particles, which was controlled by the underflow effect [31]. Adamczyk et al. [32,33] did excellent work with the hybrid Euler-Lagrange approach to deal with dense discrete phase in cyclone and circulating fluidized beds.

In this context, to better understand the motion trajectories of the particle phase during the separation process, we present a numerical study and analysis with comprehensive mathematical models, including RSM (Reynolds stress model), VOF (volume of fluid) and DPM (discretized particle model), making it possible to predict the trajectories of different particles based on the stochastic characteristic. Correlations between the forces and trajectories of the particles and the effects of material properties and operational parameters on the separation efficiency give a clear understanding of the particle motion behavior in the hydrocyclone as a method for improving its separation efficiency.

The application background of this work is tailing recovery in TiO_2 production via the sulfate process in China. The hydrocyclone recovery process is the key to improving the yield of Ti elements in ore and reducing the discharged residues. This work facilitates a deeper understanding of the effect of the forces on the particles and reveals the difference between fine and coarse particles. These findings make a remarkable contribution to the improvement of tailing recovery in this industry. Furthermore, a broader study was conducted over a wide range of particle properties and operating conditions, which make this paper helpful for TiO_2 production and also meaningful for other cyclone separation processes.

MATERIAL AND METHODS

Table 1 lists the main structural parameters of the hydrocyclone used in this study. The simulation experiments were conducted with acid hydrolysis residues discharged in TiO_2 production by the sulfate method used as raw materials. Table 2 lists the solution methods, and Table 3 lists the operating conditions for all simulations.

Table 1. Structural parameters of the hydrocyclone

Parameter	Symbol	Dimension (mm)
Diameter of the body	D_c	75
Diameter of inlet	D_i	25
Diameter of vortex finder	D_o	25
Diameter of spigot	D_u	12.5
Length of vortex finder	L_v	50
Length of cylindrical part	L_c	75

Table 2. Solution methods

Solution methods	
Pressure-velocity coupling	Simple
Spatial discretization	Second order upwind
Time step, s	5×10^{-4}
Number of grids	259,000; hexahedral

Table 3. Simulation conditions

Simulation conditions	Value
Inlet velocity, m/s	2.28
Inlet particle volume fraction, %	1.7
Overflow pressure, atm	1.0
Underflow pressure, atm	1.0
Particle density, kg/m^3	2800-3800
Medium viscosity, cp	0.5015-4.012
Inlet slurry flow rate, kg/s	0.6274-1.3627

1. Mathematical Model

In this study, turbulent flows were modeled using an RSM model, and the interface between the liquid and the air-core was described using the VOF model. The relevant equations and detailed descriptions are by Xu et al. [34].

In the modeling of the interface between the liquid and air core in a hydrocyclone, the so-called VOF free surface model is used. The VOF simulates two or more immiscible fluid phases, in which the position of the interface between fluids is of interest. The liquid and air in a hydrocyclone are immiscible, so the VOF model was selected. The model equations are shown below:

$$\frac{\partial \alpha_k}{\partial t} + u_j \frac{\partial \alpha_k}{\partial x_i} = 0 \tag{1}$$

where α_k is the volume fraction of the k^{th} phase which varies between 0 and 1 and u_j is the velocity component in direction j.

A single momentum equation is solved throughout the domain, and the resulting velocity field is shared between the two phases. This momentum equation is dependent on the volume fraction of a fluid phase with the properties ρ and μ, given by

$$\frac{\partial}{\partial t}\rho u_j + \frac{\partial}{\partial x_i}\rho u_i u_j = -\frac{\partial p}{\partial x_i} + \frac{\partial}{\partial x_j}\mu\left(\frac{\partial u_i}{\partial x_j} + \frac{\partial u_j}{\partial x_i}\right) + \rho g_i \tag{2}$$

In general, for a k-phase system, the volume fraction averaged density ρ takes on the following form:

$$\rho = \sum \alpha_k \rho_k \tag{3}$$

All other properties (e.g., viscosity) are computed in the same way. The implicit interface tracking algorithm in the VOF was used to obtain a numerical solution.

The particle kinematic behavior was determined using the DPM model based on the results of the liquid phase and air core. The buoyancy force and liquid drag force on the particles were calculated in a Lagrangian reference frame, given by the following:

$$\frac{d\vec{u}_p}{dt} = F_D(\vec{u} - \vec{u}_p) + \frac{\vec{g}(\rho_p - \rho)}{\rho_p} \tag{4}$$

where $F_D(\vec{u} - \vec{u}_p)$ is the drag force per unit particle mass and

$$F_D = \frac{18\mu}{d_p^2 \rho_p} C_D \frac{Re_p}{24} \tag{5}$$

where $\vec{u}_p$ is the particle velocity, $\vec{u}$ is the fluid phase velocity, ρ_p is the density of the particle, d_p is the diameter of the particle, C_D is the drag coefficient, and Re_p is the relative Reynolds number, which is defined as follows:

$$Re_p = \frac{\rho d_p (u_p - u)}{\mu} \quad (6)$$

The drag coefficient C_D is determined as follows:

$$C_D = a_1 + \frac{a_2}{Re_p} + \frac{a_3}{Re_p^2} \quad (7)$$

Additionally, a_1, a_2 and a_3 are constants with different values under different Reynolds number Re_p [35].

The turbulent dispersion of particles in stochastic tracking is predicted by the integration of the trajectory equations for individual particles using the instantaneous fluid velocity, $\bar{u}+u'$ along the particle path during the integration. A stochastic method (random walk model) was used to determine the instantaneous gas velocity. In the discrete random walk (DRW) model, the fluctuating velocity components are discrete piecewise constant functions of time, and their random values are held constant over an interval of time given by the characteristic lifetime of the eddies. In the discrete random walk (DRW) model, the interaction of a particle with a succession of discrete stylized fluid phase turbulent eddies is simu-

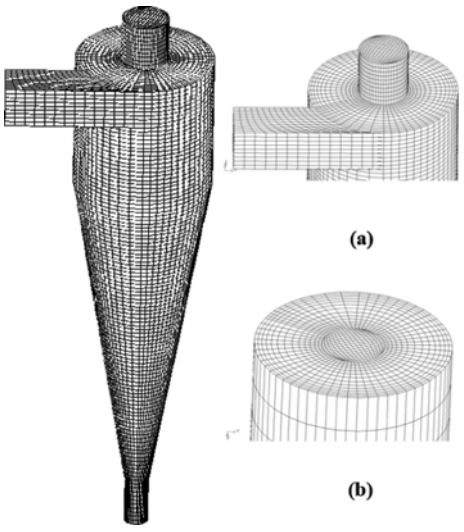

Fig. 1. Grid representation of the hydrocyclone: (a) Vortex finder and (b) spigot.

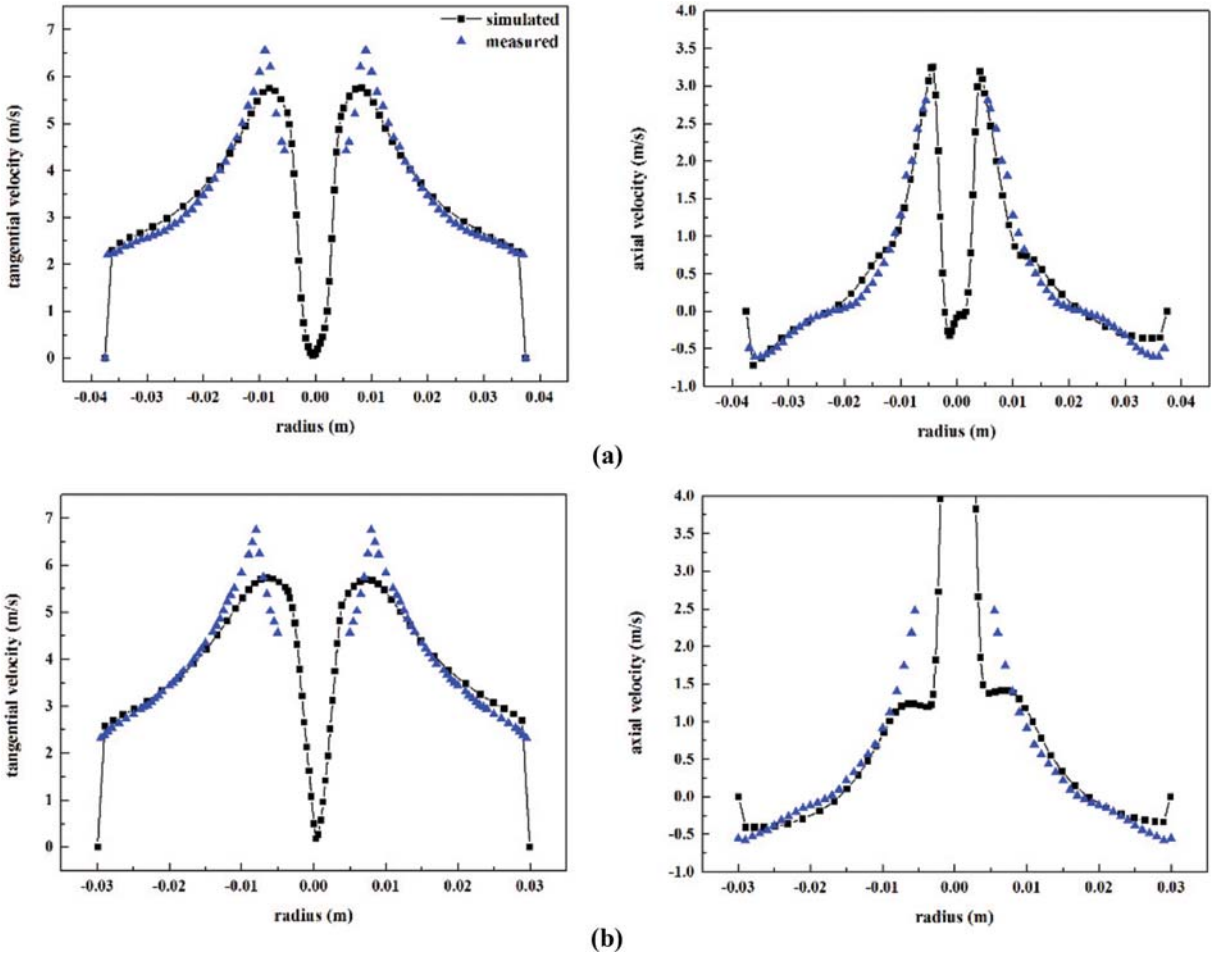

Fig. 2. Comparison of measured and simulated tangential (left) and axial (right) velocities at different locations from the top wall of a 75 mm hydrocyclone: (a) 60 mm and (b) 120 mm.

lated. Each eddy is characterized by a Gaussian distribution:

$$u' = \zeta\sqrt{\overline{u'^2}} \tag{8}$$

where ζ is a normally distributed random number, and the remainder of the right-hand side is the local root mean square value of the velocity fluctuations. Because the kinetic energy of turbulence was known at each point in the flow, these values of the root mean square fluctuating components could be defined (assuming isotropy) as follows:

$$\sqrt{\overline{u'^2}} = \sqrt{\overline{v'^2}} = \sqrt{\overline{w'^2}} = \sqrt{2k/3} \tag{9}$$

The particle was assumed to interact with the fluid phase eddy over the smaller of the eddy lifetime and the eddy crossing time.

The simulations were conducted using the Fluent CFD software package (version 16.2), with second-order upwinding and the SIMPLE pressure-velocity coupling algorithm. The convergence strategy applied the unsteady solver, and the time step was selected in the range of 10^{-4} to 5×10^{-4} s, respectively. The trial tests showed that the results were insensitive to the aforementioned range of the time step. In this model, the time step was selected as 5×10^{-4} s based on the time cost.

2. Simulation Conditions

The boundary conditions for "velocity inlet" and "pressure outlet" were considered at the inlet and outlets of the hydrocyclone, respectively. The pressure at both outlets (i.e., the vortex finder and the spigot) of the hydrocyclone was 1.0 atm, and the inlet velocity was 2.28 m/s. Fig. 1 shows the computational domain of the model divided into 259,000 unstructured hexahedral grids. The origin of coordinate system for the hydrocyclone was located at the center of the interface between the cylinder and conical sections. The trial results demonstrated that the solution was independent of the mesh size used in the numerical analysis.

RESULTS AND DISCUSSION

1. Model Validation

Fig. 2 compares the numerical results of the tangential and axial velocities on the cylindrical and conical section with Hsieh's experimental data [36] to validate our model. The profiles obtained overload the experimental points with good accuracy, although a certain amount of deviation is observed. In a similar manner, the air core diameter in Fig. 3 shows satisfactory approximation because both models were used to predict the liquid-gas flow field in the hydrocyclone. For the liquid-gas flow field, the particle behavior was obtained using the DPM model. Fig. 4 shows the efficiency obtained in the experimental and simulated analysis, with no important differences observed.

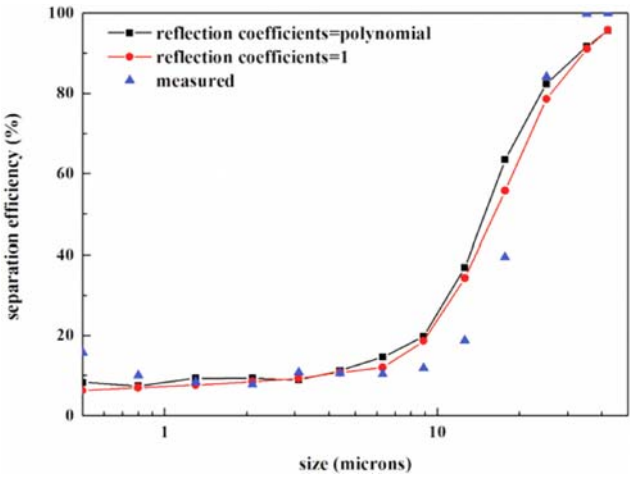

Fig. 4. Comparison of measured and simulated separation efficiencies.

2. Distribution of Particles Inside the Hydrocyclone

Fig. 5 shows the separation efficiency of the acid hydrolysis residue determined at the underflow as a function of particle size. Five characteristic points are noted, and three points, namely, the fish-hook shape and the two points at 50% and 85% efficiency, were selected to characterize the motion of the particles.

Fig. 6 shows the performance of the characteristic points simulated in the hydrocyclones for a period of 0.2 seconds to 1.2 seconds. When these particles are injected into the hydrocyclone, their motion

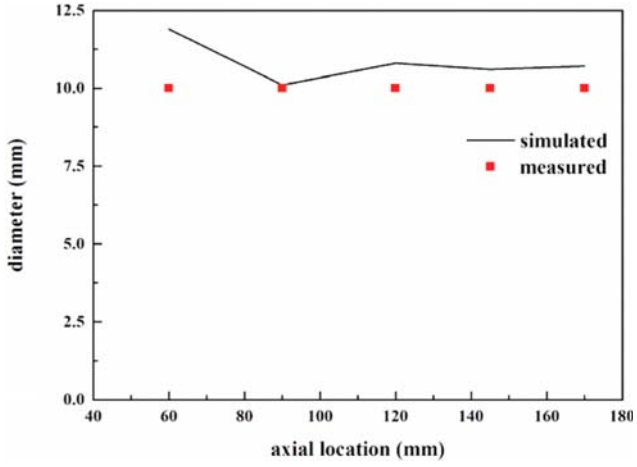

Fig. 3. Comparison of simulated and measured air core diameters.

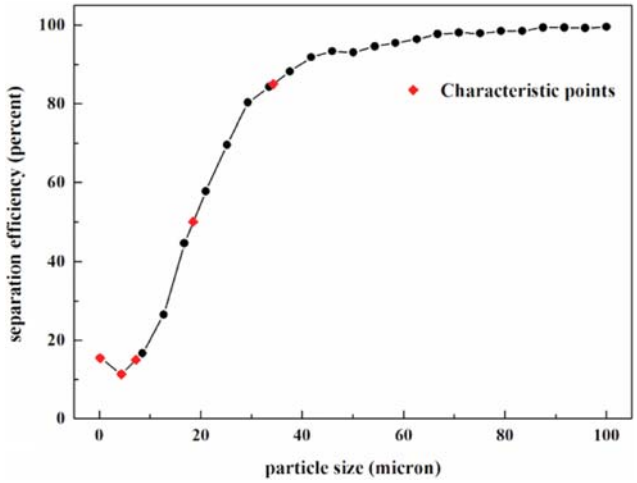

Fig. 5. Partition curve of the hydrocyclone.

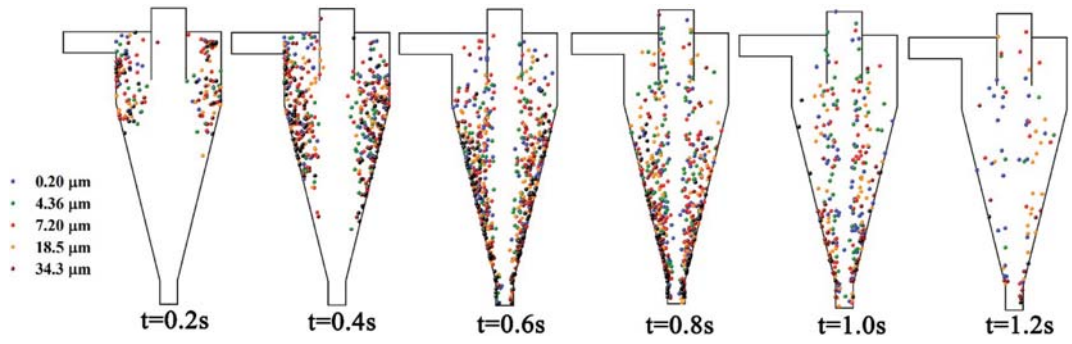

Fig. 6. Distribution of particle phase vs. time.

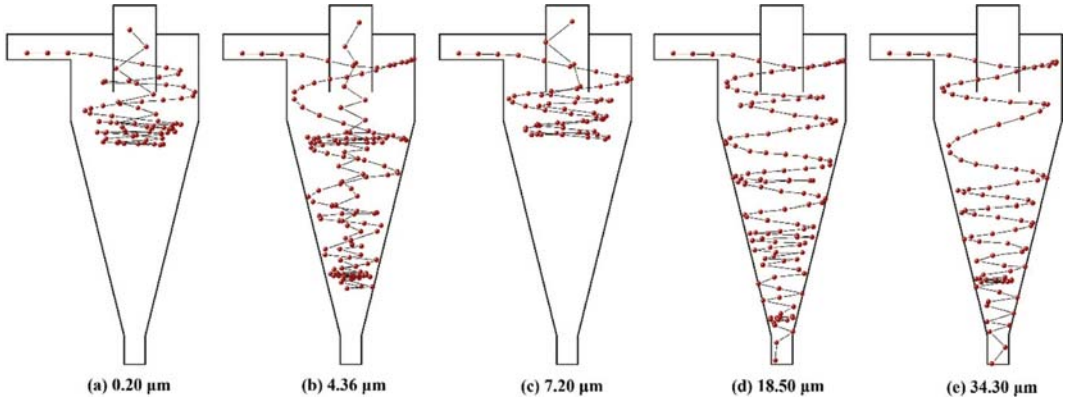

Fig. 7. Trajectories of typical particles.

trajectories are different due to the diameters and characteristic performance of both the particles and hydrocyclone structure zones. The coarse particles (34.30 μm, brown) rapidly gather near the wall and are subsequently collected on the spigot by the outer vortex under the effect of the centrifuge. The fine particles (0.20 μm, blue, 4.36 μm, green and 7.20 μm, orange) show a higher probability of passing through the locus of zero vertical velocity (LZVV) and are subsequently transported to the vortex finder by the inner vortex. The particles with the cut size (18.50 μm) produce a uniform distribution on the both sides of LZVV, and thus they have an equal chance of moving to the overflow or to the underflow outlet.

3. Forces Acting on Particles with Different Diameters

Fig. 7 shows the analysis on the trajectories of the individual particles inside the hydrocyclone. Particles with sizes of 0.20 and 7.20 μm display a short trajectory that is rotated downwards and close to the imaginary outer wall of the vortex finder. These same particles subsequently move into the inner vortex along the top of the conical section and are finally discharged into the overflow. Strangely, the trajectory of the 4.36 μm particles, which reproduce the fish-hook effects, is swept along the hydrocyclone to its lower base. These particles move to the inert vortex region and are sucked up to the top, where they blend with the fractions of the 0.20 and 7.20 μm particles at the conical section and are finally discharged from the overflow. For the particles leaving from the underflow, a 34.30 μm particle moves downwards more rapidly than an 18.50 μm particle during the interface between the conical and cylindrical portions of the hydrocyclone, as shown in Fig. 7(d) and Fig. 7(e).

Additionally, three forces were considered to control the trajectory of particles: the drag force, the pressure gradient force, and the centrifugal force. In the case of particle sizes 0.20 and 4.36 μm, Fig. 8 and Fig. 9 show the forces in three directions (tangential, radial, and axial), according to their drag force per mass (F_d), pressure gradient force per mass (F_p) and total force per mass. Note that the anti-clockwise direction is positive, the clockwise direction is negative in the tangential direction, the outward direction is positive, the inward direction is negative in the radial direction, the upward direction is positive, and the downward direction is negative in the axial direction.

Fig. 8 shows the forces on the 0.20 μm particles in these three directions. It can be observed from the analysis of the forces in the tangential and axial direction that two main types of forces exist: the drag force and the pressure gradient force. The ranges of F_d in both directions are from -1.0×10^8 m/s^2 to 1.2×10^8 m/s^2 and their orders of magnitude reached 10^8, and F_p ranged from -130 m/s^2 to 160 m/s^2 and its order was only 10^2. The difference between F_d and F_p in these two directions was as high as 10^6. Additionally, the curves of the total force in these two directions are similar to those of the drag force, which indicates that the drag force plays a dominant role. Note also that the forces on the particles in the radial direction decided the positions of the particles inside or outside the LZVV and finally followed the inner or outer vortex flow. Three types of forces are present: the drag force, the pressure gradient force and the centrifugal force in the radial direction. The order of

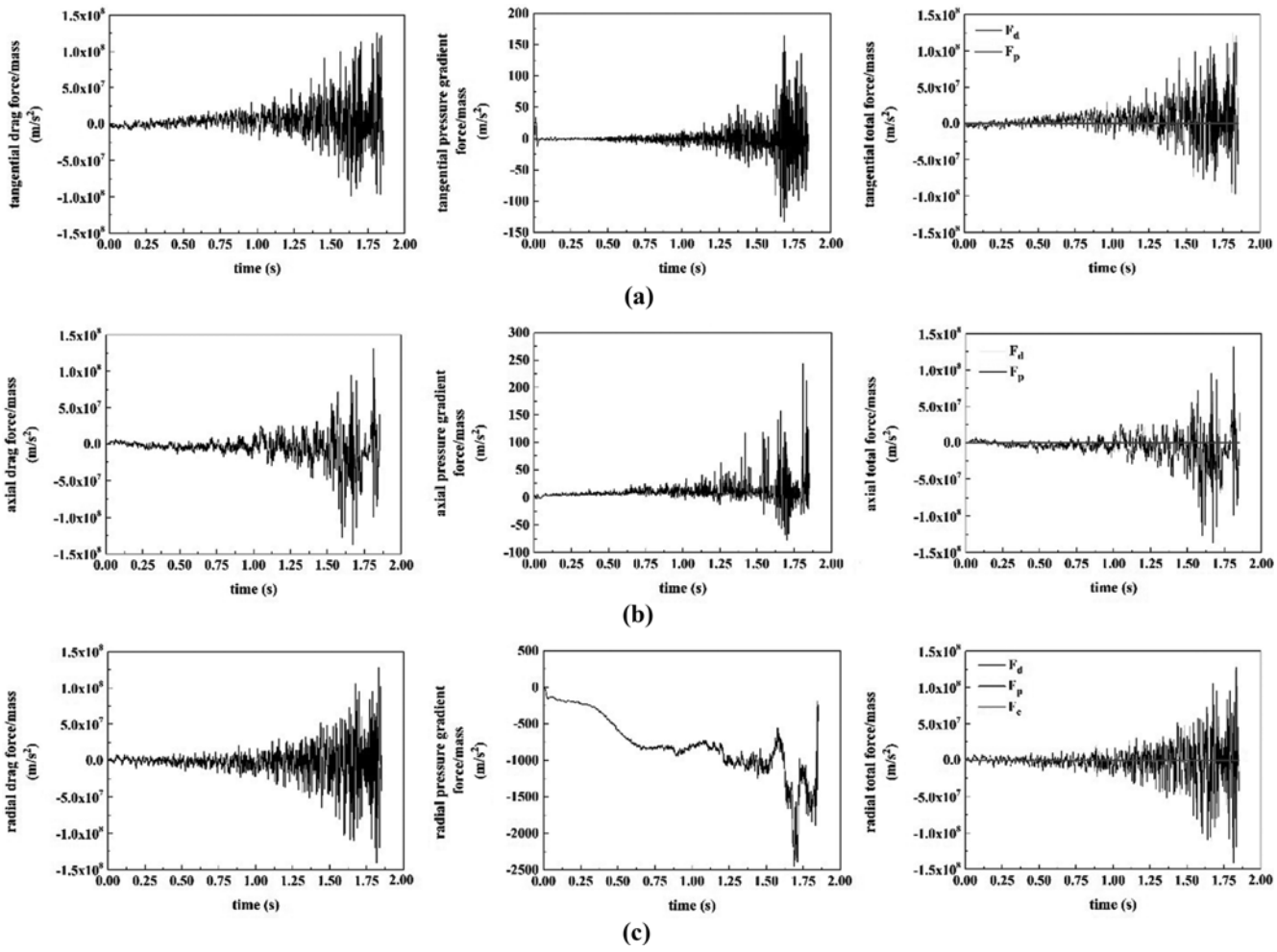

Fig. 8. Analysis of forces acting on 0.20 μm particles in the tangential (a), axial (b), and radial (c) directions.

magnitude of the drag force on the 0.2 μm particles in the radial direction reaches 10^8. The pressure gradient pressure force ranges from −2,500 to 0 m/s^2, and thus, the direction is inward. The centrifugal force in the radial direction ranges from 100 to 10,000 m/s^2, indicating that the drag force plays a leading role in the movement of the 0.20 μm particles whether in the tangential, axial or radial directions. In other words, the drag force from the liquid flow is the decisive force that controls the movement of these particles. However, due to the strong fluctuation, the particle motions exhibit a strong randomness.

Compared with the 0.20 μm particles, the order of the drag forces on the 4.36 μm particles decreases significantly to 10^5 in Fig. 9, although the drag forces on the 4.36 μm particles still play a dominant role. At the same time, the centrifugal forces on the 4.36 μm particles range from 100 to 4,100 m/s^2, values that were obviously lower than those of the 0.20 μm particles. Therefore, the finer particles, i.e., 0.2 μm, have a strong fluctuating velocity, which creates a circulatory movement between the inner and outer vortex flow and creates more possibilities of moving to the wall and discharging from the spigot. For these reasons, the separation efficiency of the 4.36 μm particles is lower than that of the 0.20 μm particles, and the fish-hook phenomenon occurs.

Further analysis of the forces acting on the 7.20, 18.50 and 34.30 μm particles was also performed, as shown in Figs. S1 through S3. The drag force exerted on the particles in the tangential and axial direction decreased exponentially as the particle size increased. The drag force had lesser influence on the coarse particles than that on the fine particles, whereas the effects of the centrifugal force and the pressure gradient force increased. Fig. S1 shows that the difference between the drag force and the pressure gradient force was 10^3, which demonstrates that the drag force has a lesser influence on the 7.20 μm particles than on the 0.20 and 4.36 μm particles, whereas the effects of the centrifugal force and the pressure gradient force increased. Hence, the 7.20 μm particles had more opportunities to move along the wall to the underflow under the influence of the centrifugal force. However, because the combined effect of the drag force and pressure gradient force in the radial direction was still stronger than the radial outward centrifugal force, which was $F_c<F_d+F_p$, only 15% of particles exited from the underflow.

For the 18.50 μm particles in Fig. S2, the drag force in the radial direction lost its influence, while the centrifugal force and the pressure gradient force continually increased. However, the pressure gradient force compelled the particle to move inwardly, and the centrifugal force acted in contrast. Calculation of the forces in the fol-

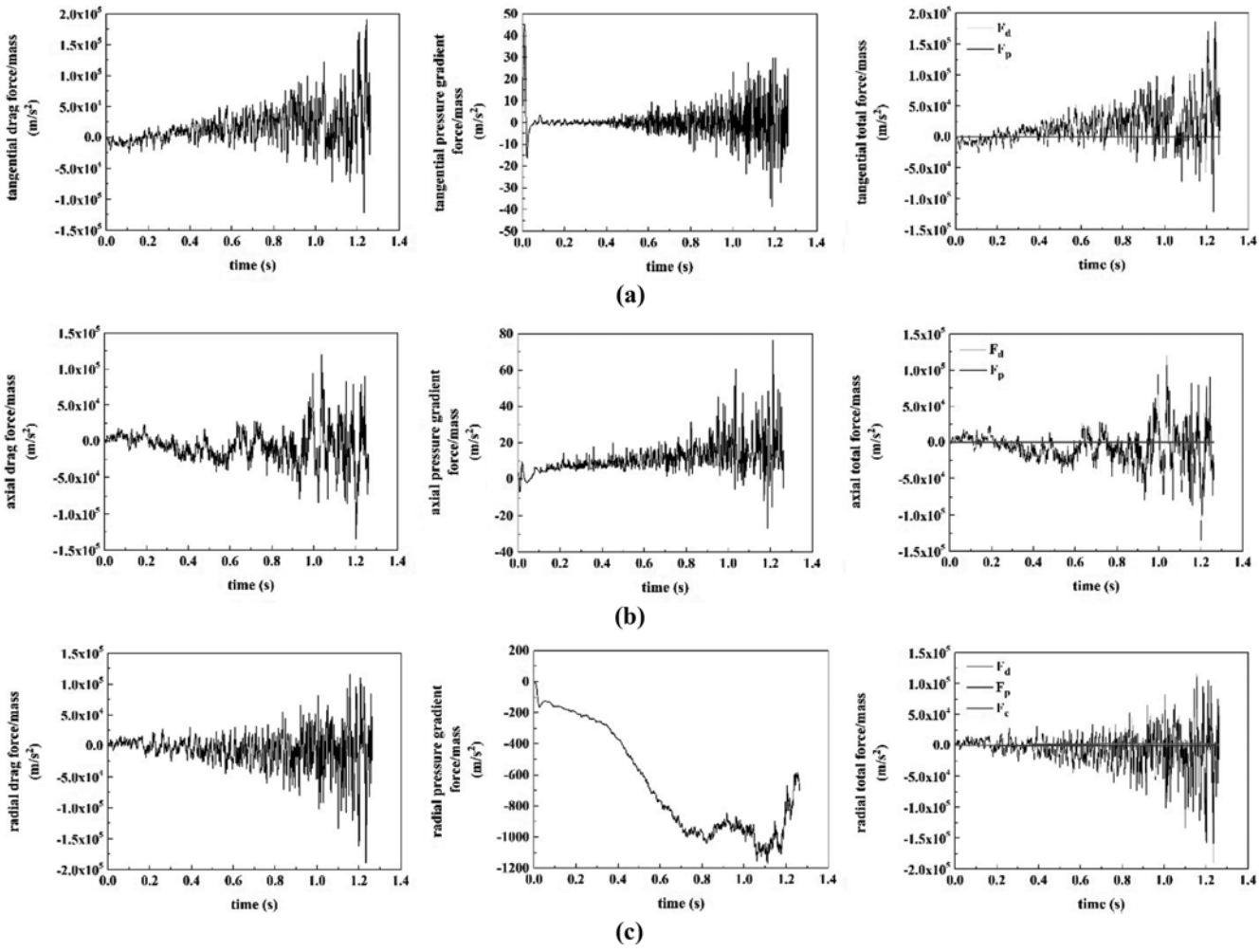

Fig. 9. Analysis of forces acting on 4.36 μm particles in the tangential (a), axial (b), and radial (c) directions.

lowing equation indicated that the joining forces on the particles were nearly zero: $F_c \approx F_d + F_p$. Therefore, the separation efficiency for the 18.50 μm particles was 50%.

The pressure gradient forces on the 34.30 μm particles in Fig. S3 became stronger, especially with the reduction of height. The calculation results showed that F_c is larger than the total amount of F_d and F_p. In this manner, the particles were easily removed in the radial direction, crossing the LZVV and discharging from the underflow.

4. Effect of Particle Density

Similar to the driving force of hydrocyclone separation, the density difference between liquid and particles has a direct influence on their action force and separation characteristics. To study the influence of the particle density, we selected five representative densities of particles in the range of 2,800-3,800 kg/m^3. The effects of the particle density on the separation efficiency are shown in Fig. 10. The particle density had no influence on the separation efficiency for 0.20 and 4.36 μm particles due to the dominant drag force of these particles in all directions. At the same time, the particle density also had no effect on the separation efficiency for the 34.30 μm particles. The separation efficiency of the 7.20 and 18.50 μm particles increased slightly with increasing densities.

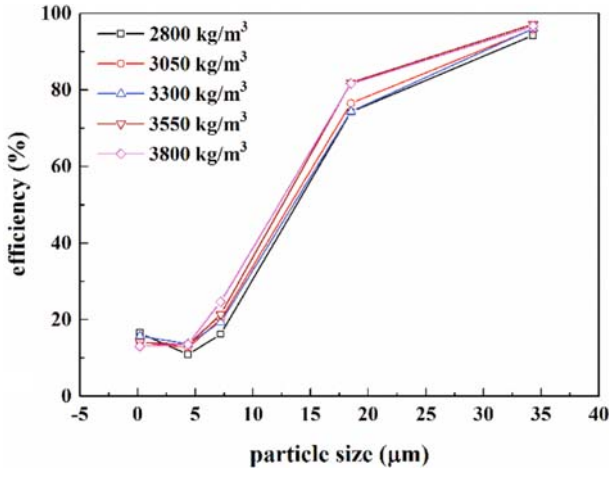

Fig. 10. Effects of particle density on separation efficiency.

Fig. 11 shows the effect of the forces on the 7.20 and 18.5 μm particles with different densities in the radial direction. For the 7.20 μm particle, density has an impact on the drag force, with a reduction of 32.2%, and the particle density increased from 2,800 to 3,800

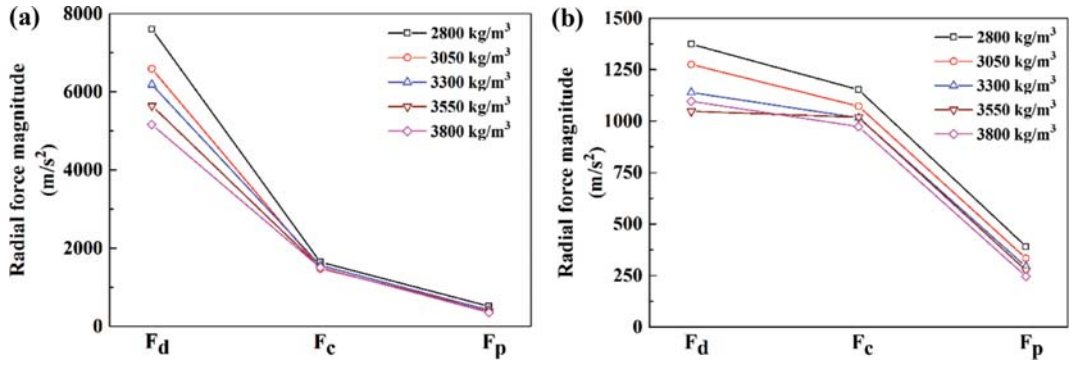

Fig. 11. Effects of particle density on the forces acting on 7.2 μm (a) and 18.5 μm (b) particles in the radial direction.

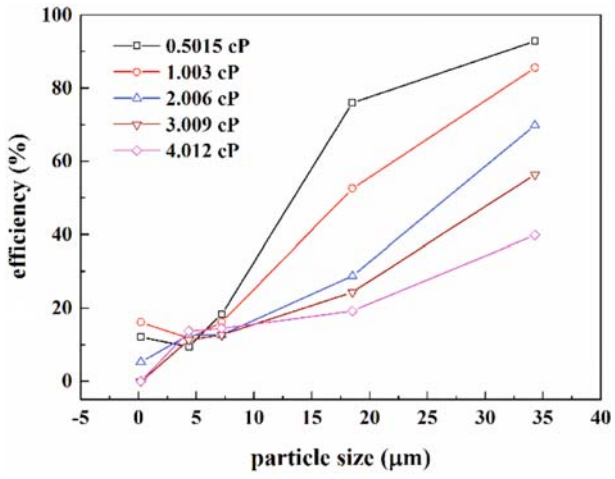

Fig. 12. Effects of slurry viscosity on separation efficiency.

kg/m^3 while the force on the pressure gradient decreased by 31.2%. The combined effect of these two forces resulted in an increasing separation efficiency with increasing particle density. Thus, all of the forces acting on the 18.5 μm particles in the radial direction showed a decreasing trend. Compared with the decrease in centrifugal force, the effect of the drag force and the pressure gradient force shows a comparative advantage, leading to increased separation efficiency.

5. Effect of Slurry Viscosity

Fig. 12 shows the effects of the slurry viscosity on the separation efficiency for a range of viscosity between 0.5015 and 4.012 cP. Compared with other particles, the changes in slurry viscosity slightly affect the separation efficiency of the 4.36 and 7.20 μm particles. However, the separation efficiency of the 0.20 μm particles decreases with the viscosity increase, and when the viscosity reaches 3.009 cP, its separation efficiency is practically null. This observation could be attributed to the increased effect of drag force on the particle movement with increasing viscosity. However, the significant effects of slurry viscosity on the particle separation efficiency for the 18.50 and 34.30 μm particles are contrary to those on the 0.20 μm particles, where the separation efficiency is strongly reduced. Fig. 13 shows the effect of the slurry viscosity on the forces acting on the particles in the radial direction. Drag forces acting on the 18.50 and 34.30 μm particles in the radial direction increase with liquid viscosity, leading to a decrease in the separation efficiency.

6. Effect of Inlet Slurry Flow Rate

In the case of the inlet flow rate, the inlet flow directly determines the intensity of the internal flow field, together with other consequences that affect the particle separation performance. If the inlet flow rate is minimum, the centrifugal force could not form. Similarly, if the flow rate is excessive, the efficiency of separation of fine particles from the vortex finder is strongly sharpened. Fig. 14 illustrates the effect of the flow of the inlet slurry on the separation efficiency. The separation efficiency of particles with sizes 0.2, 4.36 and 7.20 μm decreases as the inlet flow rate increases, opposite to the trends observed for the 18.50 and 34.30 μm particles.

The simulated results show that the increasing inlet slurry flow rate causes a significant increase in the drag force acting on the 7.20 μm particles, one that is much larger than the centrifugal force

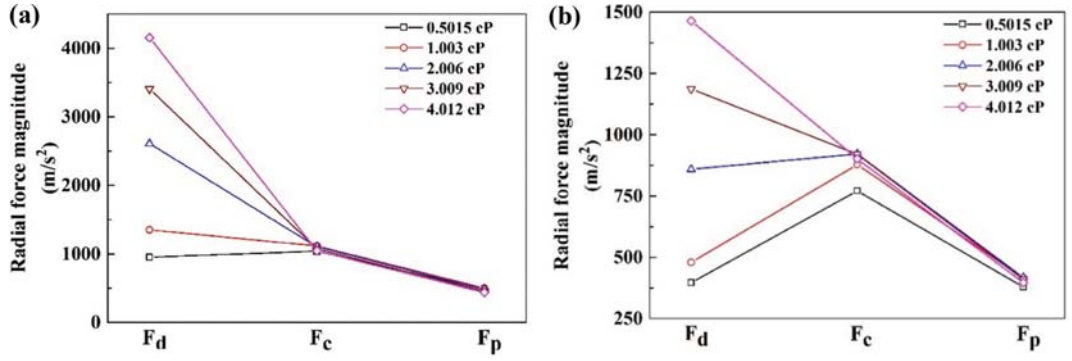

Fig. 13. Effects of slurry viscosity on the forces acting on 18.50 μm (a) and 34.30 μm (b) particles in the radial direction.

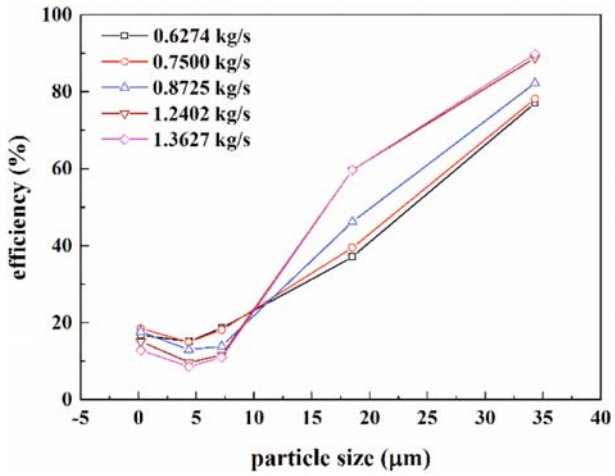

Fig. 14. Effects of inlet flow rate on separation efficiency.

and the pressure gradient force, as shown in Fig. 15(a). For the 18.50 μm particles, all of the forces acting on the particles increase with increasing inlet slurry flow rate, resulting in a change in the particle movement. For the 34.30 μm particles, the increase in the slurry flow rate enhances the influence of the centrifugal force, thus improving the separation efficiency. In addition, the slurry flow rate had a limiting value on the separation efficiency, and excess flux did not impact its efficiency, and the other forces acting on the particles are shown in Fig. 15.

CONCLUSIONS

The motion trajectories of the particle phase during the separation process were evaluated using numerical analysis with RSM, VOF and DPM. The effects of such factors, including particle density, slurry viscosity, and slurry flow rate on the separation efficiency and forces, were investigated systematically, and the principal conclusions are listed as follows. The drag force plays a leading role in the movement of the fine particles, giving the fine particles a strong fluctuating velocity. With increasing particle size, the influence of the drag force is weakened, whereas that of the centrifugal force and the pressure gradient is strengthened. The particle density has only a slight impact on the forces acting on the medium-sized particles, resulting in a slight influence on their separation efficiency. The separation efficiency of the fine particles decreased with increasing slurry viscosity. In contrast, larger particles were greatly reduced with the increase in slurry viscosity. The separation efficiency of the finer particles decreased as the inlet flow rate increased, and the reverse was true for the larger particles because the balance among the drag force, the pressure gradient force and the centrifugal force changed with the change in the inlet flow rate. The particle density, slurry viscosity and slurry flow rate impacted the behavior of the particles via the drag, pressure gradient and centrifugal forces in different ways and led to changes in the separation performance of the hydrocyclone. These results are expected to assist in setting the optimal operating conditions for various feed properties. Furthermore, by combining the CFD simulation and force analysis, a theoretical separation model can be established for reliable direction of hydrocyclone design.

ACKNOWLEDGEMENT

Foundation item: Project (51504098) supported by the National Natural Science Foundation of China.

SUPPORTING INFORMATION

Additional information as noted in the text. This information is available via the Internet at http://www.springer.com/chemistry/journal/11814.

REFERENCES

1. G. Belardi, L. Piga, S. Quaresima and N. Shehu, *Int. J. Miner. Process.*, **53**, 145 (1998).
2. L. Svarovsky, Hydrocyclones[M], Holt, Rinehart and Winston, London (1984).
3. L. R. Plitt, *CIM Bull.*, **69**, 114 (1976).
4. B. Wang and A. B. Yu, *AIChE J.*, **56**, 1703 (2010).
5. B. Wang and A. B. Yu, *Miner. Eng.*, **19**, 1022 (2006).
6. H. Yoshida, T. Takashina, K. Fukui and T. Iwanaga, *Powder Technol.*, **140**, 1 (2004).
7. S. Noroozi and S. H. Hashemabadi, *Chem. Eng. Technol.*, **32**, 1885 (2009).
8. L. G. M. Vieira, D. O. Silva and M. A. S. Barrozo, *Chem. Eng. Technol.*, **39**, 1406 (2016).
9. B. Tang, Y. Xu, X. Song, Z. Sun and J. Yu, *Trans. Nonferrous Met. Soc. China*, **27**, 1645 (2017).

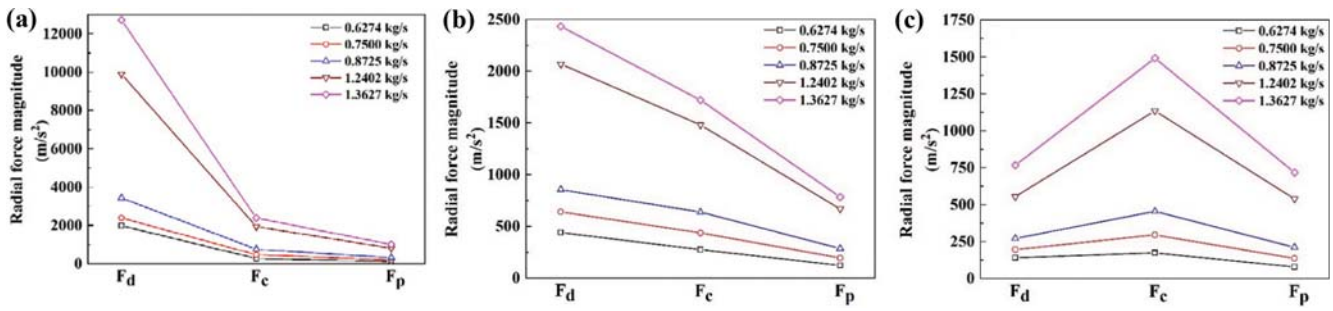

Fig. 15. Effects of split ratio on the forces acting on 7.20 μm (a), 18.50 μm (b) and 34.30 μm (c) particles in the radial direction.

10. L. G. M. Vieira and M. A. S. Barrozo, *Miner. Eng.*, **57**, 50 (2014).
11. B. Tang, Y. Xu, X. Song, Z. Sun and J. Yu, *Chem. Eng. J.*, **278**, 504 (2015).
12. I. Mokni, H. Dhaouadi, P. Bournot and H. Mhiri, *Chem. Eng. Sci.*, **122**, 500 (2015).
13. F. S. Kilavuz and Ö. Y. Gülsoy, *Int. J. Mineral. Process*, **98**, 163 (2011).
14. N. K. G. Silva, D. O. Silva, L. G. M. Vieira and M. A. S. Barrozo, *Powder Technol.*, **286**, 305 (2015).
15. M. Ghodrat, S. B. Kuang, A. B. Yu, A. Vince, G. D. Barnett and P. J. Barnett, *Miner. Eng.*, **62**, 74 (2014).
16. B. Wang and A. B. Yu, *Chem. Eng. J.*, **135**, 33 (2008).
17. L. G. M. Vieira, J. J. R. Damasceno and M. A. S. Barrozo, *Chem. Eng. Process*, **49**, 460 (2010).
18. L. Chu, W. Chen and X. Lee, *Chem. Eng. Sci.*, **57**, 207 (2002).
19. Z. Bai, H. Wang and S. Tu, *Petrol. Sci. Technol.*, **28**, 525 (2010).
20. K. Hwang, W. Wu, S. Qian and Y. Nagase, *Sep. Sci. Technol.*, **15**, 3777 (2008).
21. K. Hwang, Y. Hwang, H, Yoshida and K. Shigemori, *Powder Technol.*, **232**, 41 (2012).
22. L. Zhao, M. Jiang, B. Xu and B. Zhu, *Chem. Eng. Res. Des.*, **90**, 2129 (2012).
23. P. Fu, F. Wang, X. Yang, L. Ma, X. Cui and H. Wang, *Sci. Technol.*, **51**, 1587 (2017).
24. P. Liu, L. Chu, J. Wang and Y. Yu, *Chem. Eng. Technol.*, **31**, 474 (2008).
25. R. Cui, G. Wang and M. Li, *Trans. Noferrous Met. Soc. China*, **25**, 2422 (2015).
26. B. Cui, D. Wei, S. Gao, W, Liu and Y. Feng, *Trans. Noferrous Met. Soc. China*, **24**, 2642 (2014).
27. Z. Wang, L. Chu, W. Chen and S. Wang, *Chem. Eng. J.*, **138**, 1 (2008).
28. Y. Chang, C. G. Ilea, Ø. L. Aasen and A. C. Hoffmann, *Chem. Eng. Sci.*, **66**, 4203 (2011).
29. K. A. Nageswararao, *Chem. Eng. J.*, **80**, 251 (2000).
30. D. D. Patil and T. C. Rao, *Miner. Metall. Process*, **18**, 4 (2001).
31. K. Hwang, W. Hsueh and Y. Nagase, *Dry Technol.*, **26**, 1002 (2008).
32. P. Kozołub, A. Klimanek, R. A. Białecki and W. P. Adamczyk, *Particuology*, **31**, 170 (2016).
33. W. P. Adamczyk, K. Myöhänen, E-U Hartge, J. Ritvanen, A. Klimanek, T. Hyppänen and R. A. Białecki, *Energy*, **143**, 219 (2018).
34. Y. Xu, X. Song, B. Tang, P. Li and J. Yu, *Ind. Eng. Chem. Res.*, **52**, 5470 (2013).
35. S. A. Morsi and A. J. Alexander, *J. Fluid Mech.*, **55**, 193 (1972).
36. K. T. Hsieh, Phenomenological Model of the Hydrocyclone[D]. Ph.D. Thesis, The University of Utah, Salt Lake City, UT, U.S.A. (1988).

Supporting Information

Simulation analysis on the separation characteristics and motion behavior of particles in a hydrocyclone

Yanxia Xu, Bo Tang, Xingfu Song†, Ze Sun, and Jianguo Yu

National Engineering Research Center for Integrated Utilization of Salt Lake Resources,
East China University of Science and Technology, Shanghai 200237, China
(*Received 5 February 2018 • accepted 15 October 2018*)

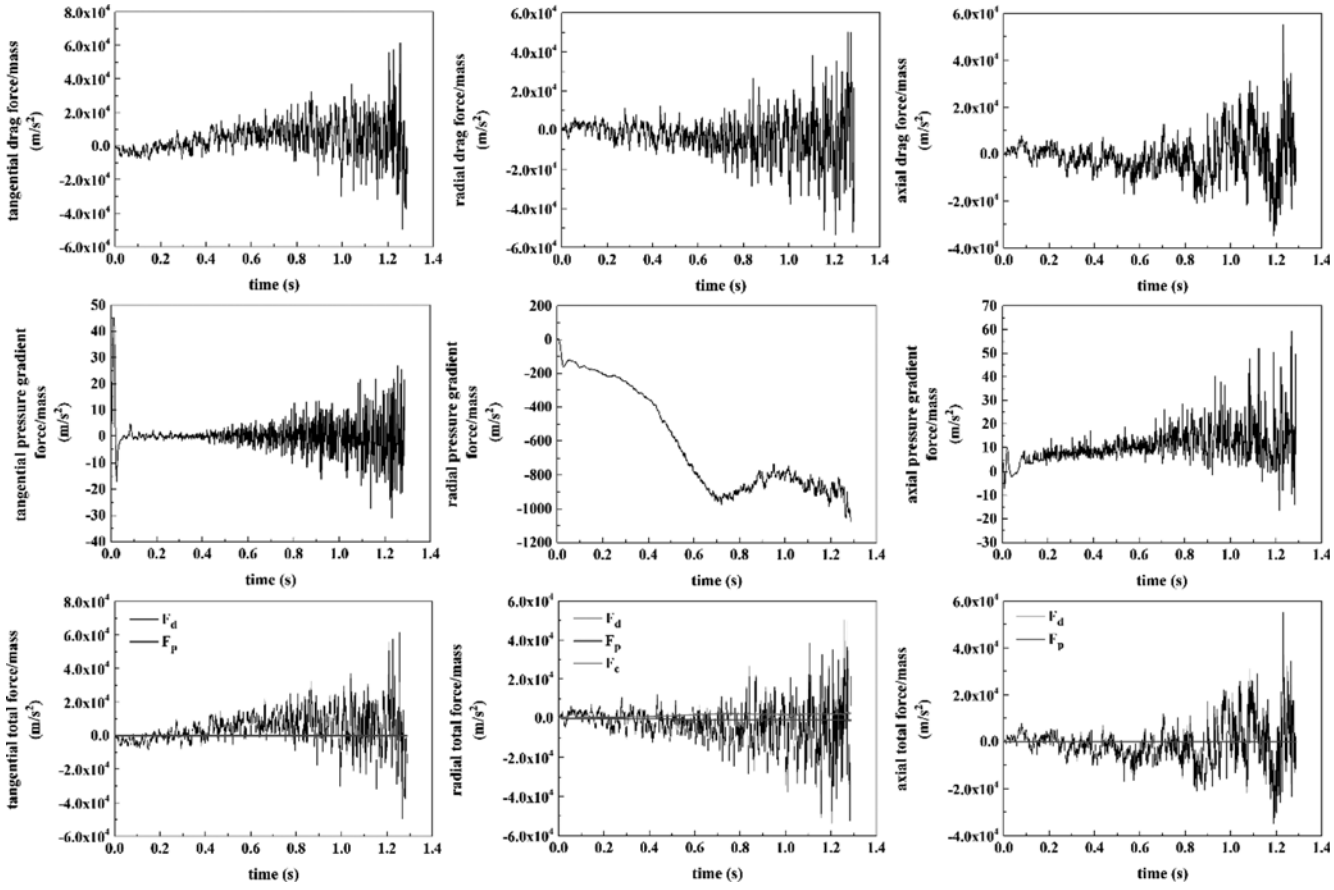

Fig. S1. Analysis of force acting on the 7.20 μm particles.

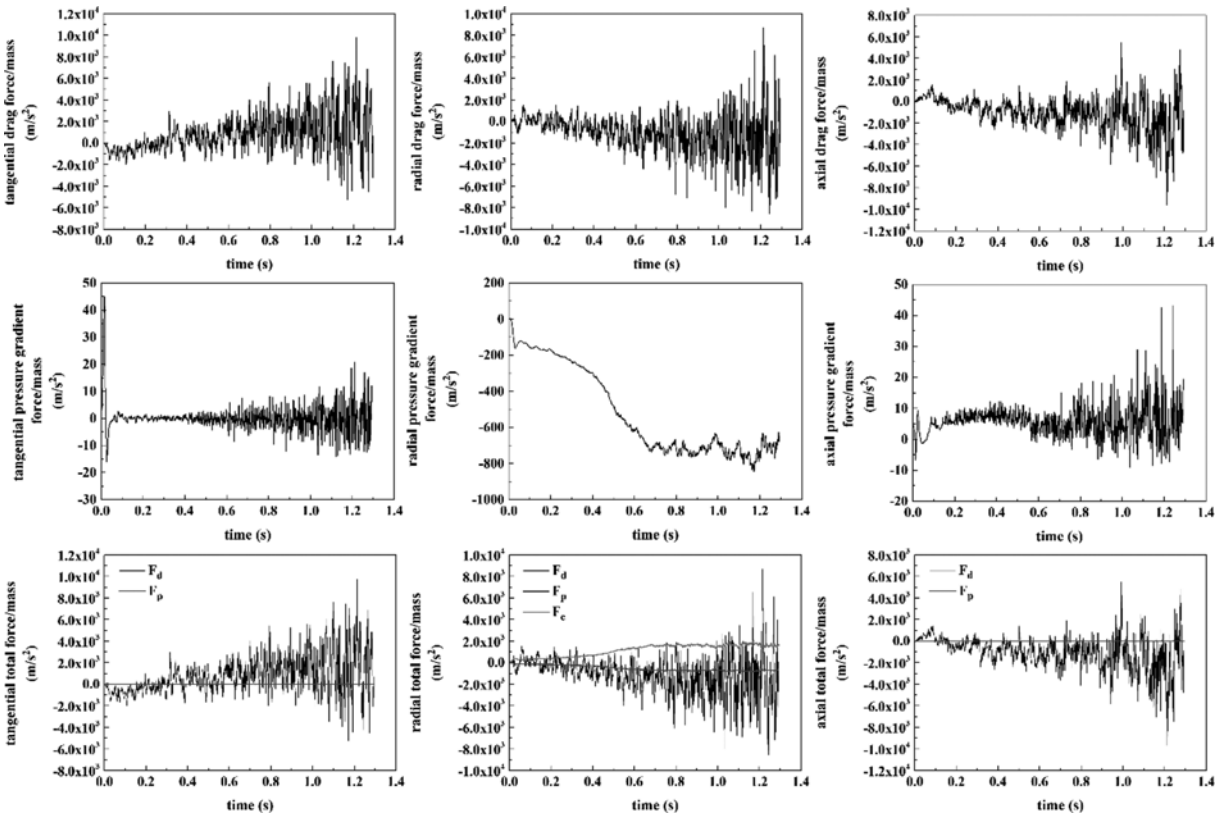

Fig. S2. Analysis of force acting on the 18.50 μm particles.

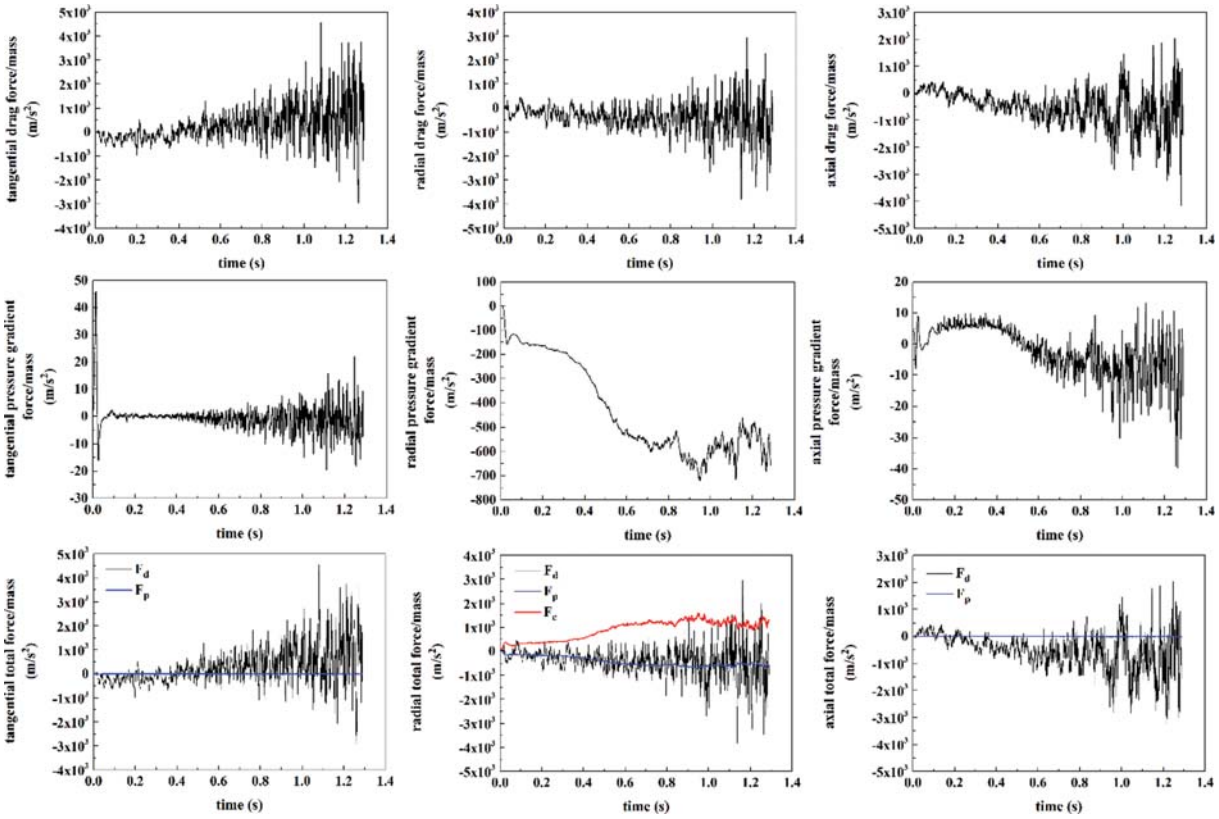

Fig. S3. Analysis of force acting on the 34.30 μm particles.